

1 Model-based data analysis of tissue growth in thin 3D printed  
2 scaffolds

3 Alexander P Browning<sup>1,2</sup>, Oliver J Maclaren<sup>3</sup>, Pascal R Buenzli<sup>1</sup>, Matthew Lanaro<sup>4</sup>,  
4 Mark C Allenby<sup>4</sup>, Maria A Woodruff<sup>†4</sup>, and Matthew J Simpson\*<sup>†1,2</sup>

5 <sup>1</sup>*School of Mathematical Sciences, Queensland University of Technology, Brisbane, Australia*

6 <sup>2</sup>*ARC Centre of Excellence for Mathematical and Statistical Frontiers, QUT, Australia*

7 <sup>3</sup>*Department of Engineering Science, University of Auckland, Auckland 1142, New Zealand*

8 <sup>4</sup>*School of Mechanical, Medical & Process Engineering, Centre for Biomedical Technologies, Queensland University of  
9 Technology, Brisbane, Australia*

10 March 26, 2021

11 **Short Title**

12 Model-based data analysis of tissue growth

13 **Abstract**

14 Tissue growth in three-dimensional (3D) printed scaffolds enables exploration and control of  
15 cell behaviour in biologically realistic geometries. Cell proliferation and migration in these  
16 experiments have yet to be explicitly characterised, limiting the ability of experimentalists  
17 to determine the effects of various experimental conditions, such as scaffold geometry, on cell  
18 behaviour. We consider tissue growth by osteoblastic cells in melt electro-written scaffolds  
19 that comprise thin square pores with sizes that we deliberately vary. We collect highly detailed  
20 temporal measurements of the average cell density, tissue coverage, and tissue geometry. To  
21 quantify tissue growth in terms of the underlying cell proliferation and migration processes,  
22 we introduce and calibrate a mechanistic mathematical model based on the Porous-Fisher  
23 reaction-diffusion equation. Parameter estimates and uncertainty quantification through  
24 profile likelihood analysis reveal consistency in the rate of cell proliferation and steady-state  
25 cell density between pore sizes. This analysis also serves as an important model verification  
26 tool: while the use of reaction-diffusion models in biology is widespread, the appropriateness  
27 of these models to describe tissue growth in 3D scaffolds has yet to be explored. We find  
28 that the Porous-Fisher model is able to capture features relating to the cell density and  
29 tissue coverage, but is not able to capture geometric features relating to the circularity of  
30 the tissue interface. Our analysis identifies two distinct stages of tissue growth, suggests  
31 several areas for model refinement, and provides guidance for future experimental work that  
32 explores tissue growth in 3D printed scaffolds.

---

\*Corresponding author. E-mail: matthew.simpson@qut.edu.au

†These authors contributed equally.

33

## Author Summary

34

Advances in 3D printing technology have led to cell culture experiments that realistically capture natural biological environments. Despite the necessity of quantifying cell behaviour with parameters that can be compared between experiments, many existing mathematical models of tissue growth in these experiments neglect information relating to population size. We consider tissue growth by cells on 3D printed scaffolds that comprise square pores of various sizes in this work. We apply a relatively simple mathematical model based on the Porous-Fisher reaction-diffusion equation to interpret highly detailed measurements relating to both the cell density and the quantity of tissue deposited. We analyse the efficacy of such a model in capturing cell behaviour seen in the experiments and quantify cell behaviour in terms of parameters that carry a biologically meaningful interpretation. Our analysis identifies important areas for model refinement and provides guidance for future data-collection and experimentation that explores tissue growth in 3D printed scaffolds.

35

36

37

38

39

40

41

42

43

44

45

46

**Keywords:** Tissue engineering; Uncertainty quantification; 3D printing; Parameter estimation; Porous-Fisher; reaction-diffusion

47

## 1 Introduction

48

49

50

51

52

53

54

55

56

57

58

59

60

61

62

63

64

65

66

67

68

69

70

71

72

73

Cell culture scaffolds provide biomimetic experimental models to explore tissue growth in essential

biological processes such as bone remodelling and development [1–3]. Achieving control over

tissue growth through these scaffolds has clinical applications such as replacing synthetic grafts

with artificially regenerated tissues [1, 4, 5]. Three-dimensional (3D) printing technology [6–9]

enables precise control of scaffold geometry, including the size and shape of the pores that

comprise each scaffold. Despite these technological advances, the effects of scaffold geometry on

scaffold-level properties of tissue growth, such as the time for tissue to close or *bridge* scaffold

pores, and individual-level properties, such as cell proliferation and migration rates, are yet to

be explicitly understood.

A preference away from traditional *in vitro* 2D culture and towards mimicking biological features, such as the bone micro-environment, through 3D scaffolds has been aided by more accurate 3D printing processes [6,7]. Technologies based on melt electrowriting [8,9] enable precise control of scaffold geometry, ensuring consistency and reproducibility. There is a significant body of research that guides the material and physical properties of scaffold construction, but a comparative scarcity on the influence of scaffold architecture on cell and tissue behaviour. In fact, several recent studies suggest that tissue growth in pore infilling experiments is strongly curvature controlled [10–13], which implies that pore shape and size play a significant role in tissue growth [11,13] since the average curvature of a pore is a function of its size [14].

In this work, we consider tissue growth by osteoblastic cells in a 3D printed scaffold formed of thin square pores with depth  $\approx 100 \mu\text{m}$  and side lengths ranging from 300 to 600  $\mu\text{m}$  (Fig. 1a–d). This thin geometry means that we can approximate the three-dimensional tissue growth as a depth-averaged two-dimensional phenomena [15]. Initially located only on the scaffold fibres, cells migrate and proliferate to form new tissue that bridges each pore over an experimental duration of 28 days (Fig. 1e–h). Scaffolds are systematically harvested and stained to obtain fluorescent microscopy images that provide highly detailed information about the pore bridging progress (which we measure as the proportion of the pore containing tissue) and the cell density

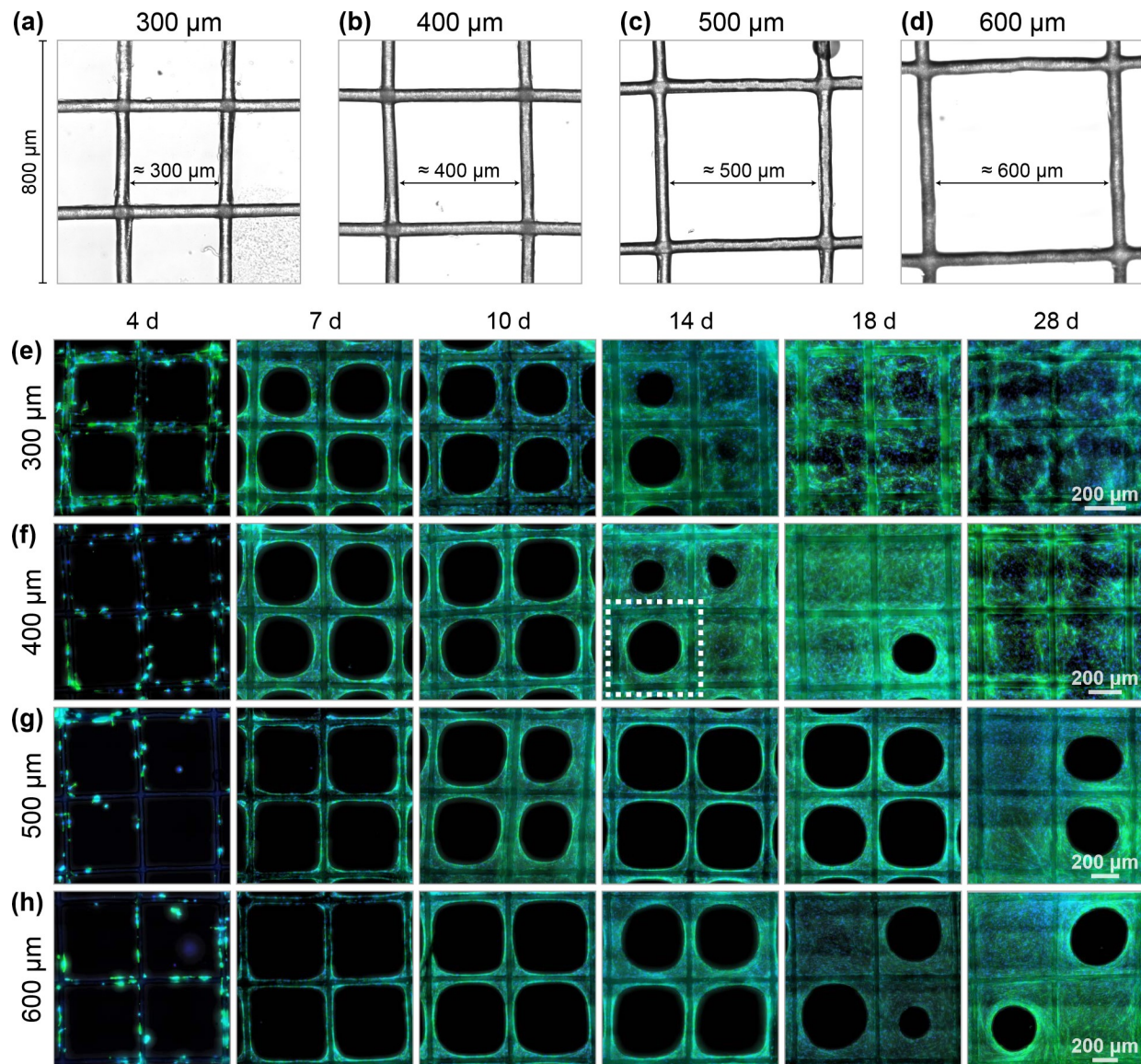


**Figure 1. Scaffold geometry and experimental data.** (a–d) Scaffolds comprise a grid of square pores with lengths ranging from 300 to 600  $\mu\text{m}$ . Shown is a  $800 \times 800 \mu\text{m}$  DIC image taken from the central region of a scaffold for each pore size. (e–h) Composite fluorescence microscopy images of pore bridging experiments. Cell nuclei, stained with DAPI, are shown in the blue channel; tissue and cytoskeleton, stained with phalloidin, are indicated in the green channel. Scale varies between pore sizes, but is identical within a pore size and is indicated in day 28 images. It is important to note that scaffolds are fixed to obtain images: data from successive time-points are independent experiments.

74 within each pore. The variability in pore bridging we see in the experimental data is striking:  
75 smaller pores appear, on average, to bridge at earlier times (Fig. 1e–f) [14]; and some, but not  
76 all, larger pores are bridged at the conclusion of the experiment (Fig. 1g–h). While we expect  
77 larger pores—which require the development of a larger amount of tissue and cells to migrate a  
78 greater distance—to bridge more slowly [14], it is unclear whether there are also changes in cell  
79 behaviour between pore sizes. We aim to determine whether there are fundamental differences  
80 in cell proliferation and migration between different pore sizes while demonstrating the value of  
81 collecting experimental data relating to both tissue coverage and cell population.

82 To disentangle the effects of cell proliferation and migration on tissue growth, we perform

83 model-based data analysis using a deterministic, continuum, process model [16]. Existing  
84 continuum models of tissue growth within porous scaffolds typically neglect information relating  
85 to properties such as cell count or density [17, 18]. Instead, the time-evolution of tissue interfaces  
86 are described using techniques ranging from continuum mechanics [3, 18, 19] to curvature  
87 flow [10, 12, 20–24]. While these models often provide good agreement with geometric features  
88 in experimental data, they yield parameter estimates that are purely phenomenological and  
89 lack a clear biophysical interpretation. We describe pore bridging using a relatively simple  
90 two-dimensional reaction-diffusion equation, often referred to as the Porous-Fisher model [14, 25].  
91 This choice naturally accounts for density-dependent behaviour expected in these experiments:  
92 contact inhibition limits cell proliferation in high-density regions, and contact stimulates cell  
93 migration, leading to co-operative tissue growth that is limited in regions of low cell density.

94 We take a summary statistic and likelihood-based approach to parameter inference [26]  
95 to identify parameters that characterise cell behaviour both individually within each pore  
96 size, and across all pore sizes simultaneously. In comparison to our previous work [14], we  
97 consider a temporal dataset that includes information about both cell density and bridging  
98 progress. To quantify the uncertainty associated with parameter estimates—which may be non-  
99 identifiable from the available information in the experimental data—we perform profile likelihood  
100 analysis [27, 28], which facilitates the computation of approximate confidence intervals [29–31].  
101 We compare parameter estimates that quantify cell proliferation and migration rates across pore  
102 sizes to determine whether pore size, and by extension, curvature, influence cell behaviour. For  
103 example, if pore size and, by extension, curvature, play a significant role in cell proliferation, we  
104 would expect the estimates of the cell proliferation rate to vary significantly between pore sizes.

105 Compared to models of 2D culture, which are well developed and routinely applied in  
106 experimental design [16, 32–36], there is little data-based modelling guidance for tissue growth  
107 within 3D scaffolds. Development and verification of mechanistic models for pore bridging  
108 is essential: models can guide engineering design choices in scaffold construction to optimise  
109 and control tissue growth [37]. Despite the widespread application of reaction-diffusion models  
110 in collective cell behaviour [32, 38–40] and biology more broadly [41–44], their suitability to  
111 describe geometrically-induced phenomena—such as that arising from corners and the relatively  
112 small, constrained, domain in our experiments—remains largely unexplored. Qualitatively, the  
113 Porous-Fisher model produces results that capture key behaviours in the experimental data;  
114 namely both an increase in cell density over the duration of the experiment, and sharp-fronted  
115 tissue growth that bridges each pore (Fig. 2). A key focus of our work is to further verify the  
116 appropriateness of the Porous-Fisher model by comparing features not used for calibration to  
117 model predictions, and comparing parameter estimate and model behaviour across pore sizes.  
118 Given that tissue growth is thought to be curvature controlled [11], we focus on comparing  
119 geometric features in the data, such as circularity, to model predictions. Comparing parameter  
120 estimates and model predictions across pore sizes is crucial for model verification: if only a single  
121 experiment condition is considered, the model might appear to match the experimental data  
122 but be incapable of matching data across multiple experimental conditions without significantly  
123 varying the parameters [35, 45]. Through this analysis, we identify several avenues for both  
124 future experimentation and model refinement.

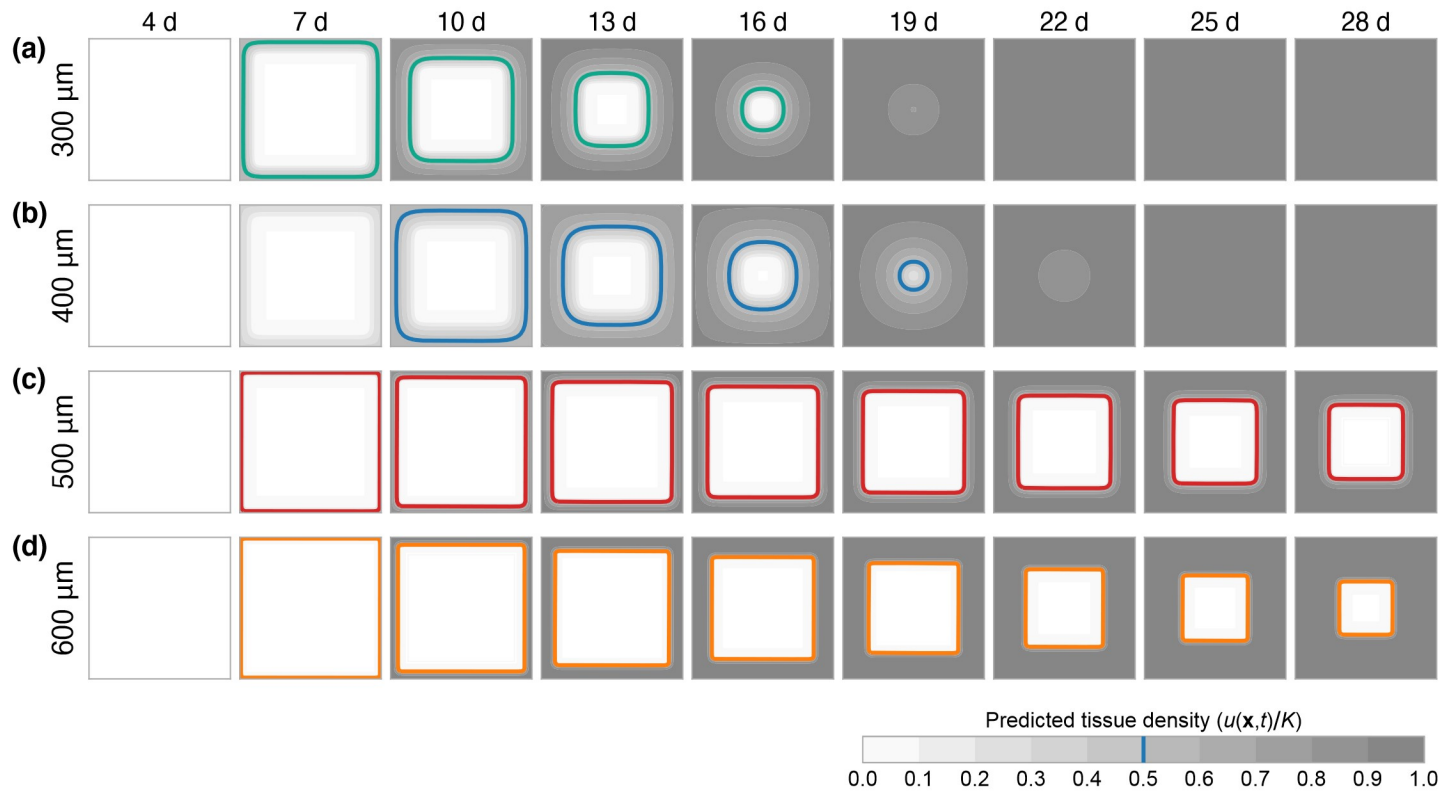


**Figure 2. Model simulated tissue growth.** Model simulation using the maximum likelihood estimate where information relating to cell density and tissue coverage are included in the likelihood. The coloured curves show the boundary of the ECM, taken to be  $\tau = 0.5$  (50%) of carrying capacity,  $K$ . Shown in greyscale is the density as a proportion of carrying capacity.

125 The outline of the work is as follows. We first describe the experimental model and methods  
 126 used to summarise the data (Section 2.1). The data are available on GitHub as supplementary  
 127 material. In Section 2.2, we describe a two-component mathematical model comprising both a  
 128 deterministic process model that describes pore bridging dynamics and a probabilistic observation  
 129 process that connects model predictions to noisy experimental observations. Subsequently, we  
 130 outline the techniques used to obtain maximum likelihood estimates and likelihood profiles  
 131 (Section 2.3). We present and discuss the results in Section 3 before outlining future experimental  
 132 and mathematical modelling recommendations in Section 4. Code to reproduce all results are  
 133 provided in the high-performance, open-source, Julia language on GitHub.

## 134 2 Methods

### 135 2.1 Pore bridging experiments

136 Polycaprolactone fibres of diameter 50  $\mu\text{m}$  are fabricated into a two-layer scaffold of size 7  $\times$  7 mm  
 137 through melt electrospinning. The resultant scaffold has an overall thickness of approximately  
 138 100  $\mu\text{m}$  (two fibre layers) and comprises square shaped pores of lengths 300, 400, 500 and 600  $\mu\text{m}$   
 139 (Fig. 1a-d). Prior to cell seeding, scaffolds are sterilised and incubated in 5% CO<sub>2</sub> overnight.

140 Murine calvarial osteoblastic cells (MC3T3-E1) [46] are cultured in  $\alpha$ -MEM, 10% fetal  
 141 bovine serum, and 1% penicillin-streptomycin (Thermo Fisher). Scaffolds are placed on top

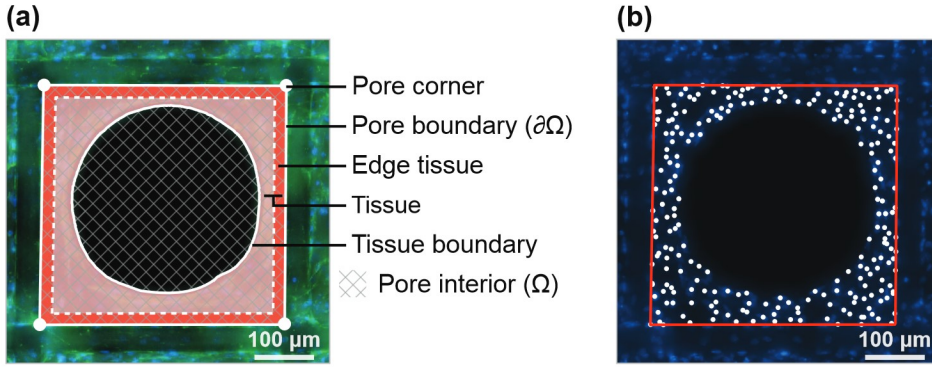


**Figure 3. Data processing technique and experimental domain.** Example data summarisation for a 400  $\mu\text{m}$  pore at day 14, indicated in Fig. 1f. (a) The pore boundary and tissue identified using the semi-automated data processing approach. Also shown is the region classified as edge tissue. In the model, we denote the boundary of the pore  $\partial\Omega$ , and the interior of the pore  $\Omega$ . (b) DAPI image, showing cell nuclei, with the pore boundary and cell locations superimposed.

142 of non-adherent 2% agarose to prevent cell-to-plate attachment within a 48-well plate. Cells  
 143 are detached using 0.05% trypsin and seeded at 7500 cells in 250  $\mu\text{L}$  media onto each scaffold  
 144 within a 48-well plate (Nunc, Thermo Fisher). Cells are allowed 4 h to attach to each scaffold  
 145 before an additional 250  $\mu\text{L}$  of media is added. Cell-seeded scaffolds are cultured in a humidified  
 146 environment at 37  $^{\circ}\text{C}$  in 5% CO<sub>2</sub> for 28 days. Media is changed every 2–3 days from day 1 to 14,  
 147 every 1–2 days from day 15 to 21, then every day from day 22 to 28. Cell viability is assessed  
 148 at day 10, 14 and 28 using calcein AM (to stain live cells) and ethidium homodimer (to stain  
 149 dead cells).

150 Cell-seeded scaffolds are fixed with 4% paraformaldehyde at day 4, 7, 10, 14, 18, and 28.  
 151 Replicates are stained with both DAPI and Alexa Fluor<sup>TM</sup> 488 Phalloidin (Thermo Fisher), which  
 152 stain cell nuclei and actin filaments, respectively. Fluorescent microscopy (Leica AF6000 LX)  
 153 is used to capture high resolution images of the centre of each scaffold. To accurately identify  
 154 scaffold geometry, a differential interference contrast (DIC) image is also captured. Fixation,  
 155 staining and microscopy are repeated across two or three replicates for each pore size and time  
 156 point. Each experimental replicate yields information about 9 to 12 pores, providing tissue  
 157 growth data across days 4 to 28 from 618 pores in total. In Fig. 1e–h we show composite images  
 158 of four pores for each pore size, for each time point.

### 159 2.1.1 Data summarisation

160 The tissue growth data are processed in a semi-automated fashion using MATLAB [47] to obtain  
 161 information about the cell population and bridging progress in each pore (Fig. 3). First, the four  
 162 corners of each pore are identified manually from the DIC image and thresholding is applied to  
 163 the phalloidin image to establish the region in each pore containing tissue (Fig. 3a). Next, the  
 164 location of the cells within each pore are identified using the thresholded DAPI image, which  
 165 colours cell nuclei (Fig. 3b). Data are discarded for pores that are not deemed sufficiently regular  
 166 in shape, or for which accurate measurements cannot be taken.

167 We summarise the experimental data obtained from each pore with four summary statistics,  
 168 denoting  $y_i^{L,t,j}$  the  $j$ th observation of the  $i$ th summary statistic at time  $t$  for a pore of size length

169  $L$ . These are as follows.

170 1. Average cell density:

$$y_1^{L,t,j} = \frac{\text{Cell count in pore}}{\text{Area of pore}}, \quad 0 \leq y_1^{L,t,j} < \infty. \quad (1)$$

171 2. Coverage:

$$y_2^{L,t,j} = \frac{\text{Area of tissue}}{\text{Area of pore}}, \quad 0 \leq y_2^{L,t,j} \leq 1. \quad (2)$$

172 3. Edge density:

$$y_3^{L,t,j} = \frac{\text{Cell count on edge tissue}}{\text{Area of edge tissue}}, \quad 0 \leq y_3^{L,t,j} < \infty. \quad (3)$$

173 Here, we define edge tissue as tissue located within approximately 20  $\mu\text{m}$  of the pore  
174 boundary (Fig. 3a).

4. Circularity:

$$\tilde{y}_4^{L,t,j} = \frac{4\pi \times \text{Area of tissue void}}{(\text{Perimeter of tissue void})^2}, \quad \pi/4 \lesssim \tilde{y}_4^{L,t,j} \lesssim 1. \quad (4)$$

$$y_4^{L,t,j} = \frac{\tilde{y}_4^{L,t,j} - 1}{1 - \pi/4} + 1, \quad 0 \lesssim y_4^{L,t,j} \lesssim 1. \quad (5)$$

175 Here,  $\tilde{y}_4^{L,t,j}$  represents the standard measure of circularity or roundness [47], which  
176 approaches unity as the tissue void approaches a perfect circle. For a square shape,  
177  $\tilde{y}_4^{L,t,j} = \pi/4$ . Since our experiments consider a scaffold that is approximately square, we  
178 normalise  $\tilde{y}_4^{L,t,j}$  to obtain  $y_4^{L,t,j}$  that still tends to unity as the tissue void approaches  
179 a perfect circle, but tends to zero as the tissue void approaches a square. To smooth  
180 out small-scale irregularities in the identified tissue shape, the convex hull of the largest  
181 contiguous tissue void is used to calculate the circularity [47].

## 182 2.2 Mathematical model

183 We interpret the pore bridging experiments with a deterministic spatio-temporal process model  
184 that aims to capture the key biological processes involved in tissue growth. To account for  
185 variability in the experimental data, we model experimental observations as normally distributed  
186 about predictions made through the process model [48–50]. In this section, we describe the  
187 process model and the probabilistic observation process used for analysis.

### 188 2.2.1 Process model

189 The substrate of the wells containing the scaffolds is coated with non-adherent agarose that does  
190 not allow cell attachment, while cells are initially adhered to the scaffold fibres. Cells, therefore,  
191 cannot move freely into the pore void. Rather, cells work together to bridge the pore through  
192 interconnecting material such as extracellular matrix and intracellular actin filaments. Therefore,  
193 traditional models of cell migration based upon linear diffusion, which do not capture the sharp  
194 tissue boundary seen in the experimental data (Fig. 1e–h), are inappropriate.

195 In this work, we assume that cells move at a rate proportional to their own density and  
 196 proliferate logistically to a maximum density of  $K$ , which we model with the Porous-Fisher [39]  
 197 equation, given by

$$\frac{\partial u}{\partial t} = D \nabla \cdot \left[ \left( \frac{u}{K} \right) \nabla u \right] + \lambda u \left( 1 - \frac{u}{K} \right), \quad \mathbf{x} \in \Omega. \quad (6)$$

198 Given that the vertical depth of the pores is small compared to the horizontal length scale,  
 199 and that we observe cells forming a thin horizontal layer of tissue that bridges each pore, we  
 200 implicitly integrate out the vertical dimension [15] so that  $\mathbf{x} = (x, y)$  and  $u(\mathbf{x}, t)$  is a depth-  
 201 averaged density, which we refer to as the cell density. In Eq. 6,  $\Omega$  the interior of the pore  
 202 (Fig. 3a) and  $\theta = (D, \lambda, K)$  are parameters that relate to the diffusivity, proliferation rate, and  
 203 carrying capacity, respectively.

204 The pore is surrounded by a fibre on which cells are initially placed approximately uniformly  
 205 so that, on the fibre,  $\nabla u = 0$ . We assume that both the proliferation rate and maximum  
 206 packing density is the same as in the pore interior. Substituting  $\nabla u = 0$  into Eq. 6 recovers a  
 207 time-dependent Dirichlet boundary condition on the edge of the pore

$$\frac{\partial u}{\partial t} = \lambda u \left( 1 - \frac{u}{K} \right), \quad \mathbf{x} \in \partial\Omega, \quad (7)$$

208 where  $\partial\Omega$  represents the pore boundary (Fig. 3a).

209 Initially, cells appear distributed exclusively on the fibre, and not in the interior of the pore.  
 210 It is not until after  $t_0 = 4$  d that cells visibly start the pore bridging process (Fig. 1a–d). We,  
 211 therefore, assume that at  $t_0 = 4$  d, cells are distributed around the pore boundary (i.e., on the  
 212 fibre) with an initial density  $u_0$ , which we assume to be unknown and, therefore, estimate for  
 213 each pore size. The initial condition is given by

$$u(\mathbf{x}, t_0) = \begin{cases} u_0, & \mathbf{x} \in \partial\Omega, \\ 0, & \mathbf{x} \in \Omega. \end{cases} \quad (8)$$

214 We solve Eq. 6–8 using a finite difference scheme based upon a discretisation with  $101^2$  mesh  
 215 points for each pore size. Due to the symmetry of the problem, we only solve Eq. 6–8 on a  
 216 quarter-domain. To integrate the resultant system of ordinary differential equations, we apply  
 217 the standard Tsit5 routine in Julia [51, 52]. Full details are available in the supplementary  
 218 material.

## 219 2.2.2 Observation process

220 Whereas output from the mathematical model is deterministic and comprises the cell density,  
 221  $u(\mathbf{x}, t)$ , as a function of space and time, the experimental observations comprise noisy observations  
 222 of four summary statistics,  $\mathbf{y}^{L,t,j} = (y_1^{L,t,j}, y_2^{L,t,j}, y_3^{L,t,j}, y_4^{L,t,j})$ . To compare model realisations  
 223 to experimental observations, we define functions that map  $u(\mathbf{x}, t)$  to summary statistics that  
 224 correspond to those that summarise the experimental data. These functions are as follows.

225 1. Average cell density:

$$\mu_1(t) = \frac{1}{L^2} \iint_{\Omega} u(\mathbf{x}, t) d\mathbf{x}, \quad 0 \leq \mu_1(t) \leq K. \quad (9)$$

226 We approximate the integral in Eq. 9 numerically using the trapezoid rule.

227 2. Coverage:

$$\mu_2(t) = 1 - \frac{A_{\text{void}}(u(\mathbf{x}, t); \tau K)}{L^2}, \quad 0 \leq \mu_2(t) \leq 1. \quad (10)$$

228 Here,  $\tau$  represents a proportion of maximum cell density,  $K$ , at which tissue becomes  
 229 visible, so that in regions where  $u(t, x, y) > \tau K$ , cells are considered part of the observed  
 230 newly formed tissue and  $A_{\text{void}}(u(\mathbf{x}, t); \tau K)$  is the area of the tissue void. In this work, we  
 231 fix  $\tau = 0.5$ , so that the tissue boundary in the model is assumed to be where the density  
 232 is 50% of the maximum [14]. To calculate the area of the tissue void,  $A_{\text{void}}(u(\mathbf{x}, t); \tau K)$ ,  
 233 we apply an interpolation method to approximate the tissue boundary (supplementary  
 234 material). This approach ensures that  $\mu_2(t)$  remains a continuous function in the parameter  
 235 space, which is desirable for computational inference.

236 3. Edge density:

$$\mu_3(t) = u(\mathbf{x}_b, t), \quad 0 \leq \mu_3(t) \leq K. \quad (11)$$

237 Here,  $\mathbf{x}_b$  is any point on the pore boundary (the modelled cell density is homogeneous on  
 238 the pore boundary); we set  $\mathbf{x}_b = (0, 0)$ .

239 4. Circularity:

$$\tilde{\mu}_4(t) = \frac{4\pi A_{\text{void}}(u(\mathbf{x}, t); \tau K)}{P_{\text{void}}^2(u(\mathbf{x}, t); \tau K)}, \quad \pi/4 \leq \tilde{\mu}_4(t) \leq 1, \quad (12)$$

$$\mu_4(t) = \frac{\tilde{\mu}_4 - 1}{1 - \pi/4} + 1, \quad 0 \leq \mu_4(t) \leq 1. \quad (13)$$

239 Here,  $P_{\text{void}}(u(\mathbf{x}, t); \tau K)$  is an interpolated approximation of the perimeter of the tissue  
 240 boundary (supplementary material). As for  $\tilde{y}_4^{L,t,j}$ , we normalise  $\tilde{\mu}_4(t)$  to obtain  $0 \leq$   
 241  $\mu_4(t) \leq 1$  (Eq. 5). For simulations where the coverage exceeds 0.99, we set  $\mu_4(t) = 1$  for  
 242 convenience.

243 To account for biological noise and measurement error, we assume that model realisations  
 244 describe the *expected behaviour* and that observations of the summary statistics are independent  
 245 and normally distributed [48]. Therefore,

$$y_i^{L,t,j} \sim \text{Normal}\left(\mu_i(t; L, \boldsymbol{\theta}), \sigma_i^2(\mu_i(t; L, \boldsymbol{\theta}))\right). \quad (14)$$

246 Here, we write  $\mu_i(t) = \mu_i(t; L, \boldsymbol{\theta})$  to emphasise the dependence of model realisations on the  
 247 pore size,  $L$ , and set of unknown parameters,  $\boldsymbol{\theta} = (D, \lambda, K, u_0)$ . We observe in Fig. 4 that the  
 248 variability in the experimental data varies significantly between both summary statistics and  
 249 observation times. Therefore, we pre-estimate a variance function,  $\sigma_i(\mu_i)$  as a function of the

mean [48]. Here, we take  $\sigma_i(\cdot)$  to be a quadratic, with intercept of 10% of the maximum standard deviation observed for the summary statistic (supplementary material).

## 252 2.3 Inference

253 We take a summary statistic, likelihood-based, approach to inference and sensitivity analysis.  
 254 Given a set of observations from pores of size  $L$ ,  $\mathbf{Y}^L = \{\mathbf{y}^{L,t,j}\}_{j,t}$ , the log-likelihood function is  
 255 given by

$$\ell(\boldsymbol{\theta}; \mathbf{Y}^L, L) = \sum_{t \in \mathcal{T}} \sum_j \sum_{i \in \mathcal{S}} \log \phi\left(y_i^{L,t,j}; \mu_i(t; L, \boldsymbol{\theta}), \sigma_i^2(\mu_i(t; L, \boldsymbol{\theta}))\right), \quad (15)$$

256 where  $\mathcal{T} = \{7, 10, 14, 18, 28\}$  is the set of observation times ( $t_0 = 4$  d is excluded from the  
 257 analysis);  $\mathcal{S} \subseteq \{1, 2, 3, 4\}$  is the set of summary statistics included in the analysis; and  $\phi(x; \mu, \sigma^2)$   
 258 is the normal density function.

### 259 2.3.1 Parameter bounds

260 The set of unknown parameters,  $\boldsymbol{\theta} = (D, \lambda, K, u_0)$ , carry a physical interpretation so we can  
 261 formulate realistic parameter bounds. The doubling time of MC3T3-E1 osteoblast cells in  
 262 two-dimensional culture is approximately 15 h [46], which corresponds to a proliferation rate  
 263 of approximately  $\lambda \approx 1.1 \text{ d}^{-1}$ . Analysis based upon the overall bridging time of MC3T3-E1  
 264 osteoblast cells suggests  $D$  carries a magnitude of approximately  $100 \mu\text{m}^2 \text{ d}^{-1}$  [14]. Results in  
 265 Fig. 4a,b suggest that cell density is bounded above by approximately  $4 \times 10^{-3} \text{ cells } \mu\text{m}^{-1}$ , which  
 266 corresponds to a packing density where a monolayer of cells occupy the same amount of space  
 267 as a disk with diameter of approximately 18  $\mu\text{m}$ . Based on these values, we choose conservative  
 268 bounds such that

$$\begin{aligned} 10 &\leq D \leq 2000 \mu\text{m}^2 \text{ d}^{-1}, \\ 1 \times 10^{-2} &\leq \lambda \leq 2 \text{ d}^{-1}, \\ 2 \times 10^{-3} &\leq K \leq 5 \times 10^{-3} \text{ cells } \mu\text{m}^{-2}, \\ 1 \times 10^{-5} &\leq u_0 \leq 2 \times 10^{-3} \text{ cells } \mu\text{m}^{-2}. \end{aligned} \quad (16)$$

### 269 2.3.2 Maximum likelihood estimation

270 We apply maximum likelihood estimation [53] to obtain a best fit parameter combination,  $\hat{\boldsymbol{\theta}}^L$ ,  
 271 for each pore size. The maximum likelihood estimate (MLE) is given by

$$\hat{\boldsymbol{\theta}}^L = \underset{\boldsymbol{\theta}}{\operatorname{argmax}} \ell(\boldsymbol{\theta}; \mathbf{Y}^L, L), \quad (17)$$

272 subject to the bounds given in Eq. 16.

273 To compute a numerical approximate the solution to Eq. 17, we employ both a global and  
 274 local optimisation routine from the open-source **NLOpt** optimisation library [54]. First, we run  
 275 a global optimisation routine, based on the **DIRECT** algorithm [55], for a fixed amount of time  
 276 (chosen to be 6 hours). This approach avoids the need to specify an initial guess of  $\boldsymbol{\theta}$  for the  
 277 optimisation routine. We then use the output from the global optimisation routine as the initial  
 278 guess in a the local optimisation algorithm **BOBYQA** [56]. We look for a maximum with absolute

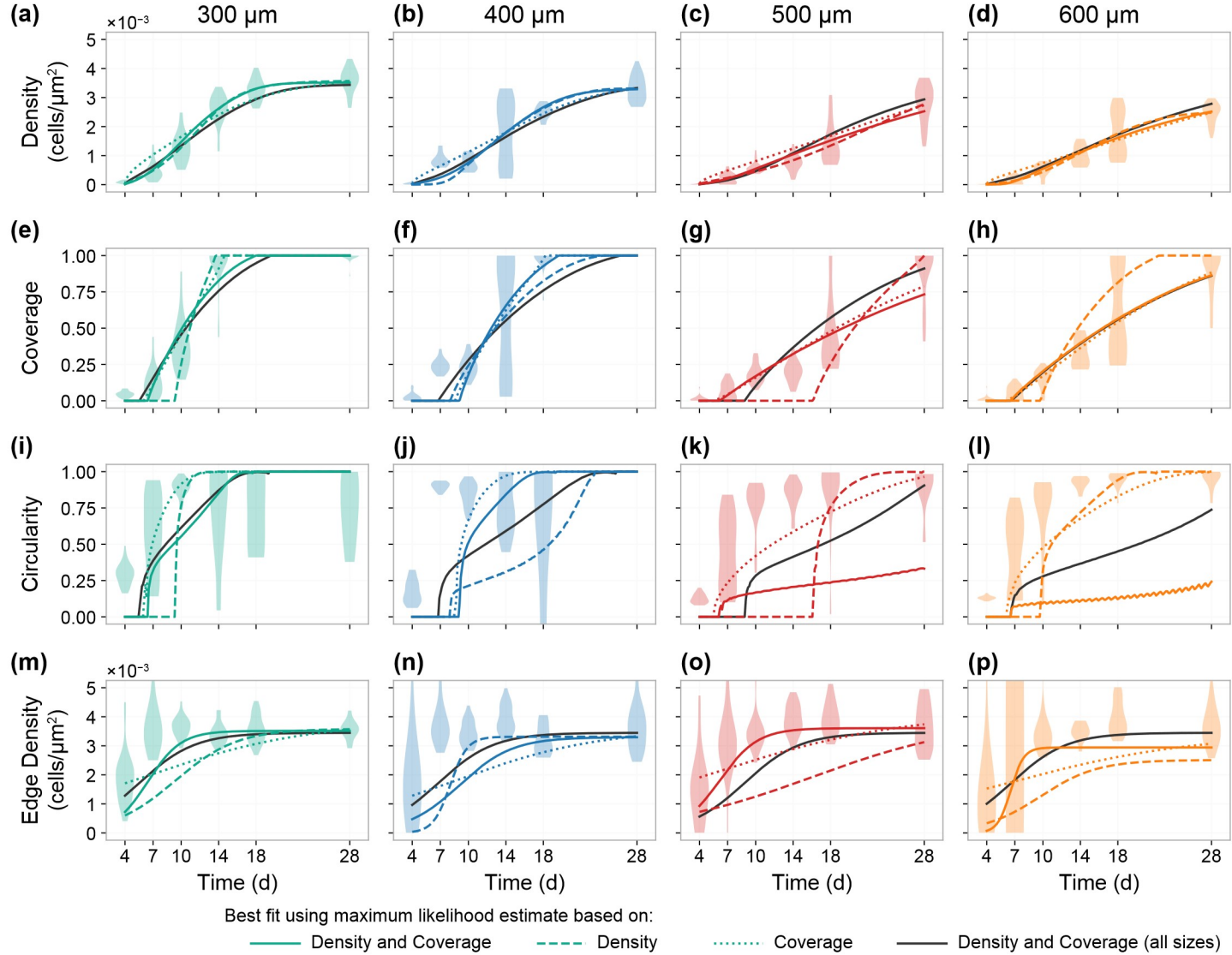


**Figure 4. Processed experimental data and model fits.** Experimental data and model fit showing (a–d) the density, (e–h) the coverage, (i–l) the circularity, and (m–p) the edge density. Violin plots show the experimental data. In each case, a model prediction is shown based on the maximum likelihood estimate that includes information relating to the cell density (dashed colour); cell density and tissue coverage (solid colour); tissue coverage with day 28 density measurements (dotted colour); and cell density and tissue coverage from all pore sizes (solid grey).

279 threshold of  $10^{-4}$ , several orders of magnitude below the threshold of 1.92 for an approximate  
280 univariate 95% confidence interval from a normalised-log-profile-likelihood [53].

281 **2.3.3 Profile likelihood analysis**

282 While point estimates provide a means of assessing the ability of the model to capture features  
283 in the data, we are interested in establishing parameter uncertainties and comparing estimates  
284 across pore sizes. To do this, we profile the log-likelihood function for each parameter [29, 30].

285 First, we partition the parameter space into a parameter (or group of parameters) of interest,  
286  $\psi$ , and nuisance parameters,  $\gamma$ , such that  $\boldsymbol{\theta} = (\psi, \gamma)$ . The profile log-likelihood for the parameter  
287  $\psi$  is given by

$$\ell_p(\psi; \mathbf{Y}^L, L) = \sup_{\boldsymbol{\lambda}} \ell(\psi, \boldsymbol{\lambda}; \mathbf{Y}^L, L). \quad (18)$$

288 For example, to profile the diffusivity, we would specify  $\psi = D$  and  $\gamma = (\lambda, K, u_0)$ . To obtain a  
289 value of  $\ell_p(D; \mathbf{Y}^L, L)$ , we maximise the log-likelihood function in the case that  $D$  is fixed.

290 Likelihood-based confidence intervals can be defined from the profile log-likelihood by an  
291 asymptotic approximation using the chi-squared distribution, for sufficiently regular problems  
292 [53, 57]. 95% confidence intervals and regions are given using the threshold values of 1.92 and  
293 3.00 log-likelihood units below the maximum for univariate and bivariate profiles, respectively  
294 [53, 57, 58]. It is convenient to work with a normalised profile log-likelihood

$$\hat{\ell}_p(\psi; \mathbf{Y}^L, L) = \sup_{\boldsymbol{\lambda}} \ell(\psi, \boldsymbol{\lambda}; \mathbf{Y}^L, L) - \ell(\hat{\theta}^L; \mathbf{Y}^L, L), \quad \hat{\ell}_p \leq 0. \quad (19)$$

295 Here, a 95% confidence interval is given where  $\hat{\ell}_p(\psi; \mathbf{Y}^L, L) \geq -1.92$ , for example [53].

296 To compute numerical approximations to each profile log-likelihood, we employ the local  
297 optimisation routine BOBYQA [56]. The log-likelihood is profiled along a regular spaced grid,  
298  $(\psi_1, \psi_2, \dots, \psi_M)$ , in series, starting at the grid point closest to the MLE, using the MLE as the  
299 initial guess [30]. Subsequent grid points use the output from the previous grid points as an  
300 initial guess. Again, we look for a maximum with absolute threshold of  $10^{-4}$ .

301 **3 Results and Discussion**

302 We interpret spatially-detailed, temporal, pore bridging data from a range of pore sizes using a  
303 relatively simple reaction-diffusion model. Our analysis considers data relating to the spatial  
304 characteristics of tissue growth—specifically, the tissue coverage and circularity of the tissue  
305 void—in addition to typical measurements, such as cell density. We aim to quantitatively  
306 determine whether there are fundamental differences in cell behaviour and tissue growth between  
307 different pore sizes, and verify the appropriateness of the reaction-diffusion model in explaining  
308 pore bridging, by comparing results across a series of experiments with various pore size. In  
309 particular, applications of reaction-diffusion models to describe tissue growth are typically limited  
310 to one-dimensional or unbounded geometries [32–36, 38–41]; there is comparatively little guidance  
311 on applying these models to describe the geometrically constrained phenomena we study.

312 In Fig. 1e–h, we show a subset of the experimental images obtained for each pore size over

313 the duration of the experiment, and in Fig. 4 we show the summary statistics collected from the  
 314 processed experimental data for each pore size. As each scaffold is fixed prior to staining and  
 315 imaging, we note that data collected from successive time points are statistically independent.  
 316 We work with average cell density (Fig. 4*a-d*) instead of cell count to allow direct comparison  
 317 between pore sizes. It is not until after day four that cells migrate from the fibres into the pore  
 318 void, so we exclude data collected at earlier time points from the analysis, and calibrate the  
 319 model with observations taken after day four. Observations from day four itself are excluded as  
 320 cells primarily occupy the fibres, which the model does not consider (Fig. 1*e-f*). By the end  
 321 of the experiment (28 days), the majority of the 300 and 400  $\mu\text{m}$  pores are bridged (85% and  
 322 100%, respectively), and the cell density appears very close to a steady-state (the average cell  
 323 densities are 102% and 93% of the edge density, respectively). In comparison, several of the 500  
 324 and 600  $\mu\text{m}$  pores do not bridge at the conclusion of the experiment (70% and 60% bridged at  
 325 day 28, respectively), and, for these pore sizes, cell growth is more evident between days 18 and  
 326 28 (cell densities are 78% and 69% of edge density, respectively).

327 Using information about the cell density and tissue coverage, we calibrate the Porous-Fisher  
 328 model to obtain a maximum likelihood estimate (MLE),  $\theta^L$ , individually for each pore size  
 329 (Table 1). We show the solution of the model at the MLE, which we refer to as the best fit,  
 330 along with the predicted tissue boundary in Fig. 2. Qualitatively, the behaviour predicted by  
 331 the model matches that seen in Fig. 1 for the experimental data. First, the Porous-Fisher model  
 332 predicts sharp-fronted migration, where regions ahead of the tissue boundary are devoid of cells.  
 333 Second, we see cell migration drive tissue growth that bridges each pore. Pore bridging appears  
 334 to occur at a slower rate for the larger pores, consistent with experimental observations. A  
 335 counter-intuitive result that highlights the variability in pore bridging we see in the experimental  
 336 data is that the 600  $\mu\text{m}$  pores are predicted to bridge faster than the 500  $\mu\text{m}$  pores: this is also  
 337 seen in the experimental data, where at day 18 tissue coverage is greater in the 600  $\mu\text{m}$  than the  
 338 500  $\mu\text{m}$  pores (Fig. 1).

339 In Fig. 4, we overlay a time-series of the best fit for each summary statistic with the  
 340 experimental data, and in Fig. 5 we compare relationships between summary statistics predicted  
 341 by the model to the experimental data. In all cases, we interpret realisations of the deterministic  
 342 process model as the expected behaviour. To determine the distinct value of collecting information  
 343 relating to the cell density and coverage, we also calculate the MLE in the case where we calibrate  
 344 the model using (i) the cell density alone, and (ii) the coverage alongside day 28 observations of  
 345 the cell density. Finally, to determine if the model can simultaneously match data across all

|                   | $D$ ( $\mu\text{m}^2 \text{d}^{-1}$ ) | $\lambda$ ( $\text{d}^{-1}$ ) | $K$ (cells/ $\mu\text{m}^2$ ) |
|-------------------|---------------------------------------|-------------------------------|-------------------------------|
| 300 $\mu\text{m}$ | 397 (290,653)                         | 0.561 (0.353,0.858)           | 0.00352 (0.00338,0.00361)     |
| 400 $\mu\text{m}$ | 1030 (525,1690)                       | 0.35 (0.191,0.694)            | 0.0033 (0.00314,0.00343)      |
| 500 $\mu\text{m}$ | 117 (40.6,269)                        | 0.497 (0.238,1.21)            | 0.00361 (0.00322,0.00401)     |
| 600 $\mu\text{m}$ | 99.9 (54.7,240)                       | 1.41 (0.621,2.0)              | 0.00294 (0.00271,0.00319)     |
| All               | 426 (364,552)                         | 0.339 (0.261,0.388)           | 0.00345 (0.00336,0.00355)     |

**Table 1.** Maximum likelihood estimates obtained by calibrating the Porous-Fisher equation to information relating to the cell density and tissue coverage. Asymptotic 95% confidence intervals, approximated using the profile likelihoods (Fig. 6) are given in parentheses. All values are stated to three significant figures.

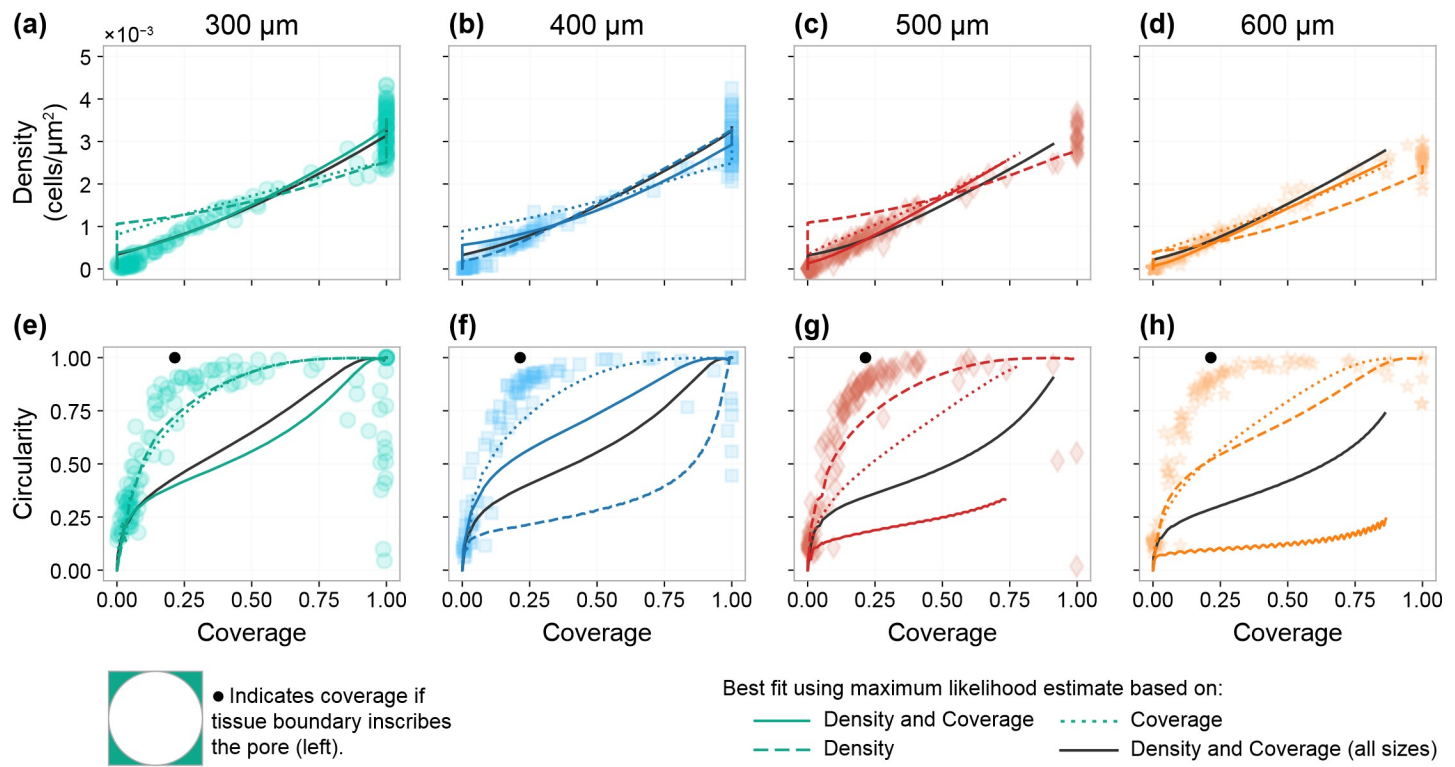


**Figure 5. Relationships between experimental and simulated summary statistics.** Experimental data and model fit showing the relationship between (a–d) tissue coverage and cell density, and (e–h) coverage and circularity. In each case, a model prediction is shown based on the maximum likelihood estimate based on the cell density (dashed colour); cell density and tissue coverage (solid colour); tissue coverage with day 28 density measurement (dotted colour); and cell density and tissue coverage from all pore sizes (solid grey).

pore sizes, we calculate the MLE using both cell density and tissue coverage information from all pore sizes (in this case, the initial density is allowed to vary between pore sizes). We show the best fits in these three additional scenarios in Fig. 4 and Fig. 5.

Results in Fig. 4a–h show a clear value in considering information relating to tissue coverage. We see an excellent match with experimental observations of cell density for all pore sizes (Fig. 4a–d), even for cases where only tissue coverage and day 28 cell density observations are used for model calibration. Overall, we also see an agreement with experimental observations of tissue coverage; however, when the model is calibrated using cell density information alone, the best fit does not appear to capture early time tissue formation correctly (Fig. 4e–h). The model also provides an excellent match to experimental cell density and coverage observations when calibrated to all pore sizes simultaneously. These results are important as the model does not explicitly incorporate geometric behaviour (aside from the initial and boundary conditions) yet is still able to capture features relating to tissue coverage and cell density in the experimental data. This agreement between the model and experimental data is not only the case when parameter estimates are allowed to vary between pore sizes, but also when a single set of parameters is used to describe data across all pore sizes.

Comparison between model fits and experimental observations in Fig. 4a–h highlight how variable experimental observations are despite a large sample size of  $n = 618$  pores: the average density and coverage for the 400  $\mu\text{m}$  pores, for example, decreases by 12% from day 7 to 10 (the

365 model monotonically increases), and observations at day 14 of the same pore size encompass  
366 observations at nearly every other time, (Fig. 4*b,f*). For this reason, we have excluded day 7  
367 observations of 400  $\mu\text{m}$  pores from results in the main text. In the supplementary material, we  
368 demonstrate that including these observations leads to results inconsistent with the other pore  
369 sizes. We address possible reasons for high levels of variability data later in the discussion.

370 A critical area in which the model fails to capture the experimental observations is in its  
371 ability to match the circularity of the tissue boundary in the larger 500 and 600  $\mu\text{m}$  pores  
372 (Fig. 4*k,l* and Fig. 2*c,d*). We further verify this by calibrating the model to information that  
373 includes circularity, finding that the model best fit in this case does not match the circularity  
374 measurements seen in the experimental data (supplementary material). In Fig. 5*e–h* we explore  
375 the relationship between tissue coverage and circularity, which we note are both non-dimensional  
376 quantities and, therefore, can be directly compared between pore sizes. The relationships  
377 observed in the experimental data are remarkably consistent both between and within pore sizes,  
378 contrasting significantly to results in Fig. 4 that show highly variable observations. Comparing  
379 the tissue boundaries predicted by the model (Fig. 2) to the experimental data (Fig. 1) reveals  
380 why this may be the case. The model predicts initial tissue growth in both the corners and  
381 edge of the pore. In comparison, tissue growth in the experiments appears to occur initially  
382 only in the corners: it is not until the tissue boundary becomes almost completely circular,  
383 with a diameter equal to the pore size, that tissue growth occurs on the pore edge. We confirm  
384 this in Fig. 5*e–h* by calculating the coverage for a hypothetical, idealised, pore that forms a  
385 circular tissue void inscribed in the pore, equal to  $100(1 - \pi/4)\%$  for all pore sizes (indicated in  
386 black). We note that since the manufacturing process never leads to pores that are perfectly  
387 square, we do not expect to see a perfectly circular pore with coverage  $100(1 - \pi/4)\%$  in the  
388 experimental data. This corner corner bridging stage of tissue growth is not included in or  
389 captured by the Porous-Fisher model (Fig. 2). To develop a better understanding of corner  
390 bridging, we suggest future mathematical and experimental work focussed on corner bridging  
391 using scaffolds with pores large enough that tissues in adjacent corner tissues do not interact  
392 and start pore bridging [17, 22].

393 Point or maximum likelihood estimates for each parameter vary across pore sizes (Table 1),  
394 yet the model is able to match experimental observations of cell density and tissue coverage  
395 across all pore sizes with a single set of parameters (Fig. 4). To allow for parameter uncertainty  
396 when comparing parameters across pore sizes, we compute profile likelihoods (Fig. 6) and  
397 approximate confidence intervals (Table 1) for each parameter. Although profile likelihoods must  
398 be interpreted with care given that they depend not only on the process model but also the noise  
399 model, they provide valuable information about the sensitivity of the likelihood estimates we  
400 obtain. This is important as the point estimates provided by the maximum likelihood estimate  
401 give no information about parameter uncertainty, sensitivity or identifiability [29]. Although  
402 point estimates for each parameter appear to vary between pore sizes (Table 1), confidence  
403 intervals (Table 1) and likelihood profiles (Fig. 6) largely overlap, providing no evidence that  
404 these parameters vary across pore sizes. MLEs obtained for the diffusivity,  $D$ , from cell density  
405 information alone are much larger than we might expect, but examination of the profile likelihoods,  
406 which provide a lower, but no upper, bounded confidence interval, indicates that  $D$  is cannot be

407 established unless information relating to tissue coverage is included. The largest discrepancy  
408 between pore sizes is seen in the diffusivity: estimates range from  $400$  to  $1000 \mu\text{m}^2 \text{d}^{-1}$ , for the  
409  $300$  and  $400 \mu\text{m}$  pores, respectively (the larger variability and inconsistencies in data for the  
410  $400 \mu\text{m}$  pores leads to a much wider confidence interval than for the  $300 \mu\text{m}$  pores), to below  
411  $200 \mu\text{m}^2 \text{d}^{-1}$  for the  $500$  and  $600 \mu\text{m}$  pores. This variability is consistent with estimates for  
412 cell diffusivities in two-dimensional culture, which often vary over several magnitudes across  
413 experimental conditions [59, 60].

414 Estimates, profiles and confidence intervals for the proliferation rate,  $\lambda$ , are remarkably  
415 consistent between pore sizes. While the model does not capture the shape of the tissue boundary,  
416 it does capture both the cell density and tissue coverage, suggesting that the crowding effects  
417 which lead to logistic growth in the experiments are also captured. In particular, our results in  
418 Fig. 6 suggest proliferation of MC3T3-E1 is similar between scaffolds of different sizes and is  
419 lower than a rate of  $\lambda \approx 1.1 \text{ d}^{-1}$  observed in two-dimensional culture [46] (this is also seen in  
420 Fig. 7). Another interesting result is the consistency in carrying capacity,  $K$ , of approximately  
421  $0.00345$  (95% combined CI:  $(0.00336, 0.00355)$ ), which corresponds to an average packing density  
422 where a monolayer of cells occupy the same amount of space as a disk with diameter of  $19 \mu\text{m}$ . An  
423 exception is for the largest  $600 \mu\text{m}$  pore, which produces an estimate much lower than the other  
424 pores (95% CI:  $(0.0027, 0.0032)$ ). While this lower estimate may be consistent with average cell  
425 density observations (Fig. 4d), the higher estimate from the combined MLE is more consistent  
426 with behaviour at the edge of the pore (Fig. 4p). In some cases, the assumption of a constant  
427 carrying capacity across the entire pore may not be appropriate. It is not clear from the data  
428 alone whether this observation is due to actual variation in carrying capacity within a pore, or  
429 because net cell growth in the centre of the pore has not yet plateaued due to crowding effects.  
430 To answer this question, data must be collected over a longer experimental duration for these  
431 larger pores.

432 In Fig. 7 we compute bivariate profiles to assess potential relationships between parameter  
433 estimates. First, examining the bivariate profiles between the proliferation rate,  $\lambda$ , and diffusivity,  
434  $D$ , in Fig. 7a–d, reveals a hyperbolic relationship. This result is consistent with previous  
435 studies that establish only the product  $D\lambda$  using information about the position of the tissue  
436 interface [14, 40], but that cannot establish individual values for these parameters. In our work,  
437 by using information relating to both cell density and tissue coverage, we are able to establish  
438 the individual values of  $D$  and  $\lambda$  within a region of compact support (a 95% confidence region is  
439 shown in Fig. 7a–d). Second, examining the bivariate profiles between the proliferation rate,  $\lambda$ ,  
440 and carrying capacity,  $K$ , highlights the information obtainable from the 28 day experiment  
441 for each pore size. On average, the larger  $500 \mu\text{m}$  and  $600 \mu\text{m}$  pores do not bridge by the  
442 conclusion of the experiment, and we see comparatively large uncertainties in both the estimated  
443 proliferation rate and estimated carrying capacity (Fig. 7g,h). In contrast, results for the smaller  
444  $300 \mu\text{m}$  and  $400 \mu\text{m}$  pores—the majority of which bridge by day 18—show that we are able to  
445 establish these parameters with a relatively small region (Fig. 7e,f). Although point estimates  
446 for the proliferation rate vary across pore sizes (Table 1), the bivariate profiles show a significant  
447 overlap in possible parameter values, indicating that these parameters are similar between pore  
448 sizes.

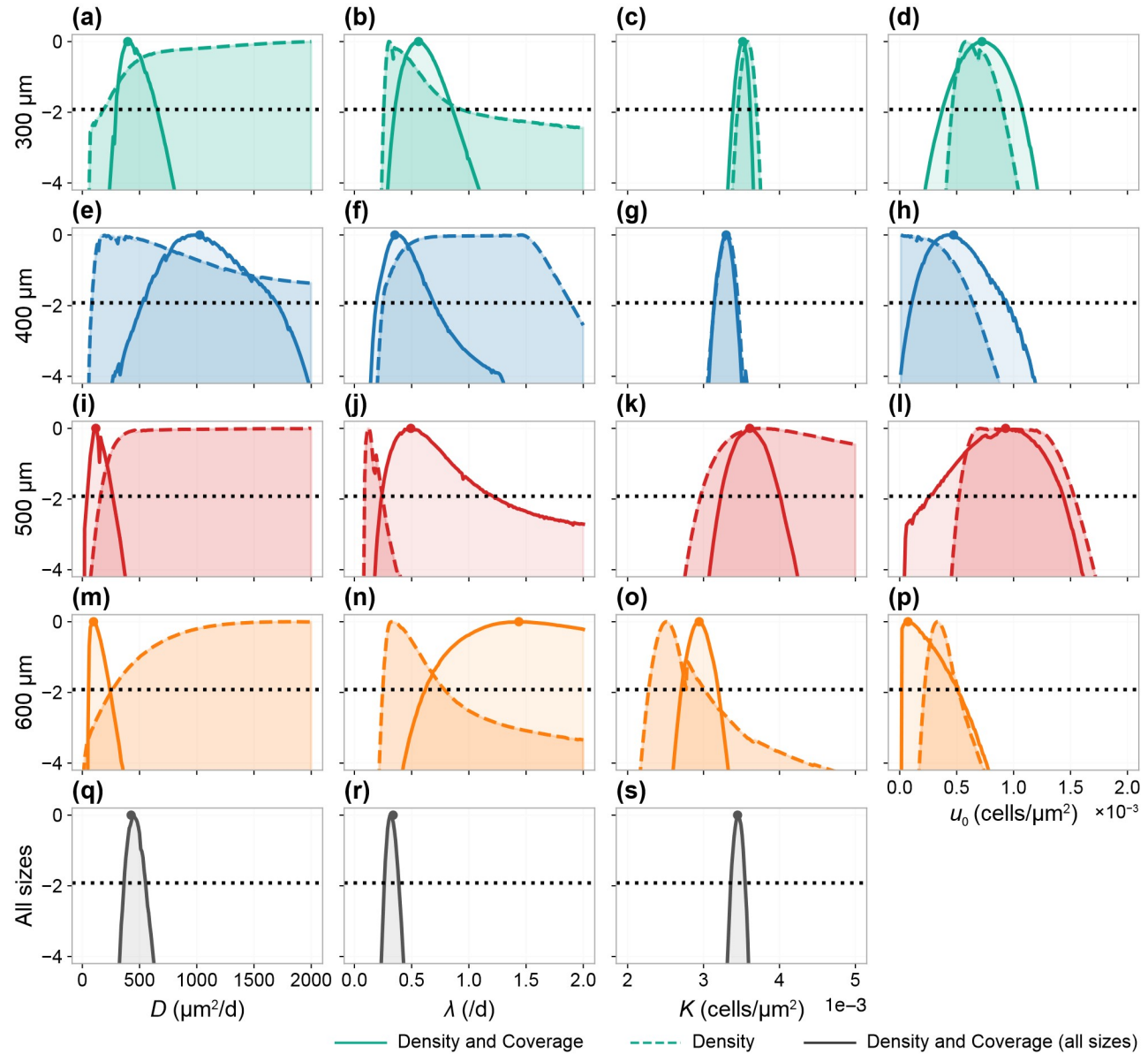


**Figure 6. Profile likelihoods for calibrated model parameters.** Profile likelihoods for each inferred parameter and pore size where only the density is used (dashed) and where both the density and coverage are used (solid). Dotted horizontal black line indicates the  $-1.92$  contour which corresponds to an asymptotic 95% confidence interval for each parameter. Also shown are profiles for  $D$ ,  $\lambda$  and  $K$  where information relating to cell density and tissue coverage information from all pores is included simultaneously.

When the data are analysed as summary statistics that depend upon time, as in Fig. 4, we see a large amount of variability that cannot be fully captured by the observation noise process we define in Section 2.2.2. However, when relationships between summary statistics of each pore are analysed with respect to each other, independent of time, we see notably less variability (Fig. 5). These results suggest that time alone is a poor predictor of each summary statistic. In contrast, the dependence between summary statistics in Fig. 5 suggests that summary statistics have well defined relationships with relatively little variability. In the deterministic process model, the initial condition (which describes the expected value of each summary statistic on day 4) is taken to be a fixed density of cells distributed around the fibres. The majority of the variability in the temporal pore bridging data may be due to variability in the initial condition, which affects initial pore formation. For example, we expect tissue growth to be slower, or stationary, for pores that initially have a smaller density of cells distributed around the pore boundary at day 4. One way around the limitation of providing a homogeneous initial distribution of the cells in the experiments is to collect time-series data, where the same pore is imaged at multiple time points. There are two ways this information could be incorporated into the mathematical model. First, by including a time delay parameter for each data point that describes the delay until tissue formation inside the pore begins, that can be profiled out as a nuisance parameter in the analysis. Second, by capturing the variability directly by describing pore bridging as a differential equation where the initial density at the pore boundaries is a random variable.

Our results do not suggest significant differences in cell behaviour between pore sizes. Despite the Porous-Fisher model not explicitly incorporating geometric behaviour (aside from the initial and boundary conditions), we can capture information relating to both tissue coverage and cell density even when calibrated simultaneously to data from all pore sizes. By accounting for tissue coverage, we quantify a similar proliferation rate for all sizes based on a logistic growth assumption. The relationship between tissue boundary circularity and coverage is similar between all pore sizes. In all pores we see two stages of bridging: first, the corners bridge—this takes longer in the larger pores—and form an approximately circular tissue boundary; second, the pore closes and remains approximately circular in shape. These observations have also been made for triangular and hexagonally shaped pores [20], and convex pores [11]. Further experimental and modelling work is needed to disentangle the effect of each of these stages on overall pore bridging and tissue growth. For example, we suggest experimental work that investigates corner bridging and tissue establishment using non-constrained or “open” geometries [17, 22], rather than the current geometry where tissue growth eventually closes a pore of finite size. To reduce overall variability in the data, variability in the initial condition should be accounted for through time-series imaging, where information about each pore is available at multiple time-points, and throughout each distinct stage.

Our thin three-dimensional experimental framework, and two-dimensional depth-averaged mathematical modelling framework, carry several advantages over more complex alternatives. In addition to information relating to tissue coverage, we are able to access detailed information about cell density, which we interpret with a mathematical model that quantifies cell behaviour with biophysical parameters such as proliferation and migration rates. This allows for comparison of cell behaviour between cell lines, allowing tissue growth optimisation with respect to cell line in

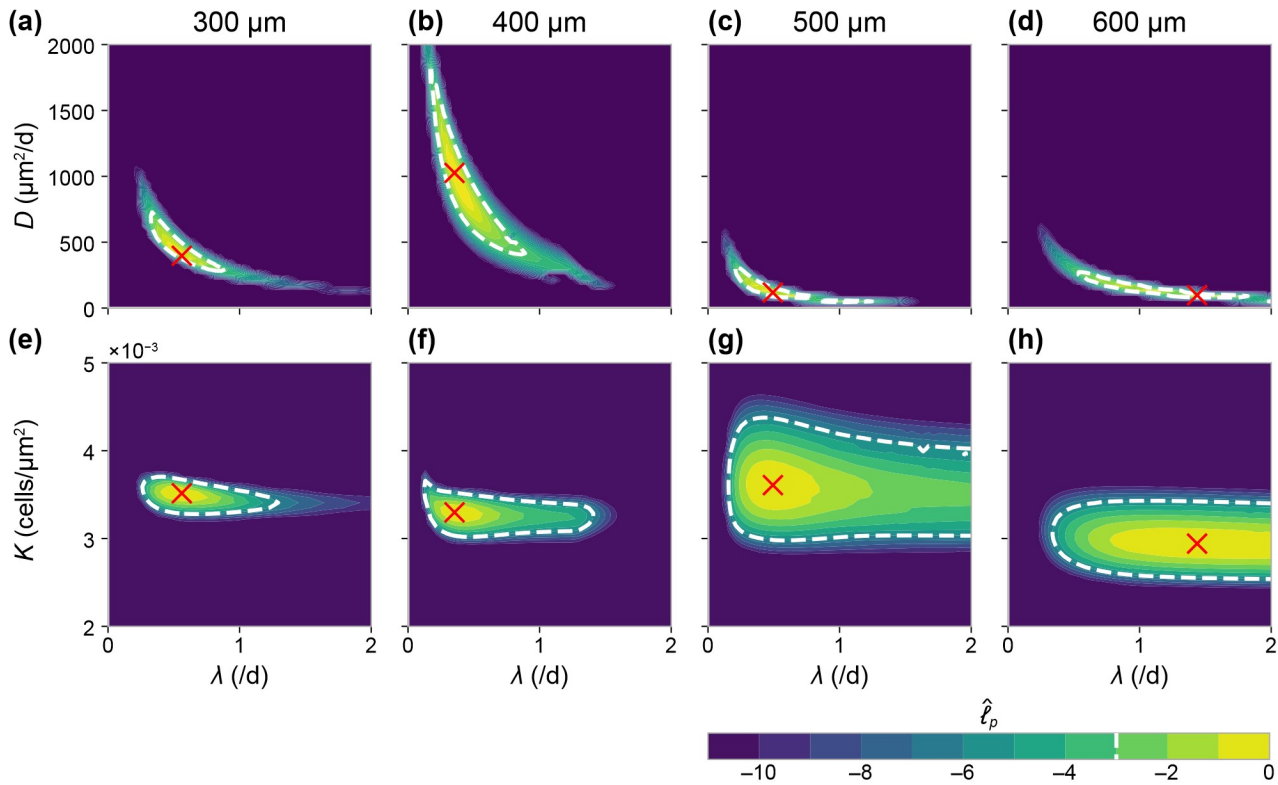


**Figure 7. Bivariate profile likelihoods for calibrated model parameters.** Bivariate profile likelihoods showing the relationship between estimates for (a–d)  $D$  and  $\lambda$ , and (e–h)  $\lambda$  and  $K$ . Dotted white lines indicates the  $-3.00$  contours which corresponds to an approximate asymptotic 95% confidence region for each parameter combination.

addition to scaffold geometry. Our modelling framework is also extensible to co-culture systems that include multiple cell lines, which are more representative of *in vivo* tissue growth, through a coupled system of partial differential equations. Additionally, working with a thin three-dimensional experimental geometry reduces the need to account for additional extraneous factors on cell growth, such as nutrient availability. For example, typical *in vitro* three-dimensional tissue culture lack the vascular system that ensures homogeneous nutrient availability for *in vivo* tissue growth [3]. In comparison, our geometry results in a monolayer of cells that are all in direct contact with growth medium.

We suggest, in future, a hybrid modelling framework to describe each stage of pore bridging, rather than a single model that captures all stages of growth. While our analysis does not preclude generalisations of the Porous-Fisher model from capturing geometric features like circularity, reaction-diffusion models alone cannot account for both the corner bridging and pore closing stages of growth we see in the experimental data. Models based on continuum mechanics or curvature control have been successful in recapturing the initial stages of bridging seen experimental data [11, 20, 23], but typically neglect information relating to cell density. Once a circular tissue boundary is established, tissue growth may be quantified using density-dependent models such as those based on the Porous-Fisher equation, or agent based models [45, 61].

## 508 4 Conclusion and Outlook

509 We analyse experimental data from a series of pore bridging experiments using a relatively  
510 simple reaction-diffusion model based on the Porous-Fisher equation. In addition to commonly  
511 reported tissue coverage information, our model allows for the interpretation of information  
512 relating to cell density, and we see a clear value in considering both measurements. For example,  
513 the cell migration rate is often unidentifiable from information relating to cell density alone  
514 but becomes identifiable when information relating to tissue coverage is included. Compared  
515 to existing models of tissue growth that are largely phenomenological [17, 18], our framework  
516 characterises cell behaviour with parameters that carry a biologically meaningful interpretation,  
517 such as cell proliferation and migration rates. We find no evidence to suggest that cell behaviour  
518 is dependent upon pore size. The cell proliferation rates, which are lower than that observed  
519 for two-dimensional culture, and carrying capacities are found to be remarkably similar across  
520 different pore sizes. This outcome suggests that our experimental protocols lead to consistent,  
521 reproducible tissue growth. This conclusion is not apparent without interpretation of the  
522 experimental data with a mechanistic mathematical model.

523 Our analysis identifies two distinct stages of pore bridging that are consistent between pore  
524 sizes: an initial corner bridging stage, and a latter hole closing stage. The Porous-Fisher model  
525 does not describe the initial corner bridging stage and, therefore, does not reproduce the shape  
526 of the tissue boundary. However, the model does match features relating to cell population and  
527 tissue coverage, thus capturing crowding effects and providing confidence in the estimated cell  
528 proliferation rates. We suggest that a better understanding of pore bridging can be formed  
529 through distinct theoretical models and experimental analysis that individually capture both  
530 the corner bridging and hole closing stages.

531 The experimental data used for model calibration suggests, at first, that pore bridging is  
532 a highly variable process. However, analysis of the relationships between summary statistics  
533 reveals this may not be the case. Rather, variability in both the initial distribution of cells on  
534 the scaffolds and corner bridging leads to a time-delay that cannot be accounted for with the  
535 information available from our data-collection method. These results highlight a potential value  
536 in designing an experiment to collect time-series observations, which will provide information  
537 about cell density and tissue coverage of each pore at multiple time points. This more detailed  
538 information will allow for the inclusion of more complicated mechanisms, such as directed  
539 migration through chemotaxis [43, 62], mechanical effects at the tissue boundary [63, 64], or the  
540 depletion of nutrients available to the cell population. At present, we find the complexity of the  
541 mathematical model is well suited to the level of information available in the experimental data,  
542 and we expect identifiability issues to arise if we were to interpret the current data with a more  
543 complex model.

544 Many of our conclusions could not have been made without considering data from multiple  
545 experimental geometries. The smaller pores, for example, give the impression that the model  
546 captures geometric features of pore closing; the inability of the model to capture these features  
547 is only evident when we analyse data for the larger pores. Comparing parameter estimates  
548 and profile likelihoods across experimental conditions is essential for constructing and verifying  
549 theoretical descriptions of pore bridging. Typical applications of mechanistic mathematical

550 models to understand tissue formation usually involve working with a single experimental  
551 geometry, most often in a one-dimensional setting. These approaches cannot provide insight  
552 into the effect of high-dimensional geometric phenomena, such as corners, which we explore in  
553 our work.

554 In conclusion, our Porous-Fisher model successfully captures many of the key features of the  
555 experiments, providing a straightforward means of interpreting experimental observations in  
556 terms of the underlying cell proliferation and migration mechanisms that drive tissue growth.  
557 To the best of our knowledge, these mechanisms have never before been explicitly characterised  
558 for tissue growth in 3D-printed scaffolds.

## 559 Data availability

560 Code and data used to produce the numerical results are available as a Julia module on GitHub  
561 at [github.com/ap-browning/Pore-Bridging](https://github.com/ap-browning/Pore-Bridging).

## 562 Funding

563 O.J.M. is supported through the University of Auckland, Faculty of Engineering James and Hazel  
564 D. Lord Emerging Faculty Fellowship. M.C.A. is supported by an Advance Queensland Fellowship  
565 (AQIRF1312018). M.J.S. is supported by the Australian Research Council (DP200100177).

## 566 Author Contributions

567 A.P.B. performed the data analysis, implemented the mathematical model, and wrote the paper.  
568 A.P.B. and M.L. processed the experimental data. M.L. and M.C.A. performed the experiments.  
569 All authors provided feedback and gave approval for final publication.

## 570 References

- 571 [1] Hollister SJ. Porous scaffold design for tissue engineering. *Nature Materials*. 2005;4(7):518–524.  
572 doi:10.1038/nmat1421.
- 573 [2] Roseti L, Parisi V, Petretta M, Cavallo C, Desando G, Bartolotti I, et al. Scaffolds for bone tissue  
574 engineering: state of the art and new perspectives. *Materials Science and Engineering: C*. 2017;78:1246–1262.  
575 doi:10.1016/j.msec.2017.05.017.
- 576 [3] Ambrosi D, Amar MB, Cyron CJ, DeSimone A, Goriely A, Humphrey JD, et al. Growth and remodelling  
577 of living tissues: perspectives, challenges and opportunities. *Journal of The Royal Society Interface*.  
578 2019;16(157):20190233. doi:10.1098/rsif.2019.0233.
- 579 [4] Barthes J, Özçelik H, Hindié M, Ndreu-Halili A, Hasan A, Vrana NE. Cell microenvironment engineering  
580 and monitoring for tissue engineering and regenerative medicine: the recent advances. *BioMed Research  
581 International*. 2014;2014:1–18. doi:10.1155/2014/921905.
- 582 [5] Mao AS, Mooney DJ. Regenerative medicine: Current therapies and future directions. *Proceedings of the  
583 National Academy of Sciences*. 2015;112(47):14452–14459. doi:10.1073/pnas.1508520112.
- 584 [6] Groll J, Boland T, Blunk T, Burdick JA, Cho DW, Dalton PD, et al. Biofabrication: reappraising the  
585 definition of an evolving field. *Biofabrication*. 2016;8(1):013001. doi:10.1088/1758-5090/8/1/013001.

- 586 [7] Forrestal DP, Klein TJ, Woodruff MA. Challenges in engineering large customized bone constructs. *Biotechnology and Bioengineering*. 2017;114(6):1129–1139. doi:10.1002/bit.26222.
- 587
- 588 [8] Paxton NC, Ren J, Ainsworth MJ, Solanki AK, Jones JR, Allenby MC, et al. Rheological characterization  
589 of biomaterials directs additive manufacturing of strontium-substituted bioactive glass/polycaprolactone  
590 microfibers. *Macromolecular Rapid Communications*. 2019;40(11):1900019. doi:10.1002/marc.201900019.
- 591 [9] Paxton NC, Allenby MC, Lewis PM, Woodruff MA. Biomedical applications of polyethylene. *European  
592 Polymer Journal*. 2019;118:412–428. doi:10.1016/j.eurpolymj.2019.05.037.
- 593 [10] Bidan CM, Kommareddy KP, Rumpler M, Kollmannsberger P, Bréchet YJM, Fratzl P, et al. How linear  
594 tension converts to curvature: geometric control of bone tissue growth. *PLOS One*. 2012;7(5):e36336.  
595 doi:10.1371/journal.pone.0036336.
- 596 [11] Bidan CM, Kommareddy KP, Rumpler M, Kollmannsberger P, Fratzl P, Dunlop JWC. Geometry as a factor  
597 for tissue growth: towards shape optimization of tissue engineering scaffolds. *Advanced Healthcare Materials*.  
598 2013;2(1):186–194. doi:10.1002/adhm.201200159.
- 599 [12] Alias MA, Buentzli PR. Osteoblasts infill irregular pores under curvature and porosity controls: a hypothesis-  
600 testing analysis of cell behaviours. *Biomechanics and Modeling in Mechanobiology*. 2018;17(5):1357–1371.  
601 doi:10.1007/s10237-018-1031-x.
- 602 [13] Callens SJP, Uyttendaele RJC, Fratila-Apachitei LE, Zadpoor AA. Substrate curvature as  
603 a cue to guide spatiotemporal cell and tissue organization. *Biomaterials*. 2020;232:119739.  
604 doi:10.1016/j.biomaterials.2019.119739.
- 605 [14] Buentzli PR, Lanaro M, Wong CS, McLaughlin MP, Allenby MC, Woodruff MA, et al. Cell proliferation and  
606 migration explain pore bridging dynamics in 3D printed scaffolds of different pore size. *Acta Biomaterialia*.  
607 2020;114:285–295. doi:10.1016/j.actbio.2020.07.010.
- 608 [15] Simpson MJ. Depth-averaging errors in reactive transport modeling. *Water Resources Research*. 2009;45(2).  
609 doi:10.1029/2008wr007356.
- 610 [16] Treloar KK, Simpson MJ, McElwain DLS, Baker RE. Are *in vitro* estimates of cell diffusivity and  
611 cell proliferation rate sensitive to assay geometry? *Journal of Theoretical Biology*. 2014;356:71–84.  
612 doi:10.1016/j.jtbi.2014.04.026.
- 613 [17] Bidan CM, Wang FM, Dunlop JWC. A three-dimensional model for tissue deposition on complex  
614 surfaces. *Computer Methods in Biomechanics and Biomedical Engineering*. 2013;16(10):1–15.  
615 doi:10.1080/10255842.2013.774384.
- 616 [18] Gamsjäger E, Bidan CM, Fischer FD, Fratzl P, Dunlop JWC. Modelling the role of surface stress  
617 on the kinetics of tissue growth in confined geometries. *Acta Biomaterialia*. 2013;9(3):5531–5543.  
618 doi:10.1016/j.actbio.2012.10.020.
- 619 [19] Salbreux G, Jülicher F. Mechanics of active surfaces. *Physical Review E*. 2017;96(3):032404.  
620 doi:10.1103/physreve.96.032404.
- 621 [20] Rumpler M, Woesz A, Dunlop JWC, Dongen JT, Fratzl P. The effect of geometry on three-dimensional  
622 tissue growth. *Journal of the Royal Society Interface*. 2008;5(27):1173–1180. doi:10.1098/rsif.2008.0064.
- 623 [21] Guyot Y, Papantonio I, Chai YC, Bael SV, Schrooten J, Geris L. A computational model for cell/ECM  
624 growth on 3D surfaces using the level set method: a bone tissue engineering case study. *Biomechanics and  
625 Modeling in Mechanobiology*. 2014;13(6):1361–1371. doi:10.1007/s10237-014-0577-5.
- 626 [22] Ehrig S, Schamberger B, Bidan CM, West A, Jacobi C, Lam K, et al. Surface tension determines tissue  
627 shape and growth kinetics. *Science Advances*. 2019;5(9):eaav9394. doi:10.1126/sciadv.aav9394.
- 628 [23] Lee HG, Park J, Yoon S, Lee C, Kim J. Mathematical model and numerical simulation for tissue growth on  
629 bioscaffolds. *Applied Sciences*. 2019;9(19):4058. doi:10.3390/app9194058.
- 630 [24] Alias MA, Buentzli PR. A level-set method for the evolution of cells and tissue during curvature-  
631 controlled growth. *International Journal for Numerical Methods in Biomedical Engineering*. 2020;36(1):e3279.  
632 doi:10.1002/cnm.3279.

- 633 [25] McCue SW, Jin W, Moroney TJ, Lo KY, Chou SE, Simpson MJ. Hole-closing model reveals exponents for  
634 nonlinear degenerate diffusivity functions in cell biology. *Physica D: Nonlinear Phenomena*. 2019;398:130–140.  
635 doi:10.1016/j.physd.2019.06.005.
- 636 [26] Browning AP, Haridas P, Simpson MJ. A Bayesian sequential learning framework to parameterise continuum  
637 models of melanoma invasion into human skin. *Bulletin of Mathematical Biology*. 2019;81(3):676—698.  
638 doi:10.1007/s11538-018-0532-1.
- 639 [27] Campbell DA, Chkrebtii O. Maximum profile likelihood estimation of differential equation parameters  
640 through model based smoothing state estimates. *Mathematical Biosciences*. 2013;246(2):283–292.  
641 doi:10.1016/j.mbs.2013.03.011.
- 642 [28] Wieland FG, Hauber AL, Rosenblatt M, Tönsing C, Timmer J. On structural and practical identifiability.  
643 arXiv. 2021;2102.05100.
- 644 [29] Raué A, Kreutz C, Maiwald T, Bachmann J, Schilling M, Klingmüller U, et al. Structural and practical iden-  
645 tifiability analysis of partially observed dynamical models by exploiting the profile likelihood. *Bioinformatics*.  
646 2009;25(15):1923–1929. doi:10.1093/bioinformatics/btp358.
- 647 [30] Boiger R, Hasenauer J, Hroß S, Kaltenbacher B. Integration based profile likelihood calculation for PDE  
648 constrained parameter estimation problems. *Inverse Problems*. 2016;32(12):125009. doi:10.1088/0266-  
649 5611/32/12/125009.
- 650 [31] Simpson MJ, Baker RE, Vittadello ST, Maclareen OJ. Practical parameter identifiability for spatio-  
651 temporal models of cell invasion. *Journal of The Royal Society Interface*. 2020;17(164):20200055.  
652 doi:10.1098/rsif.2020.0055.
- 653 [32] Sengers BG, Please CP, Oreffo ROC. Experimental characterization and computational modelling of two-  
654 dimensional cell spreading for skeletal regeneration. *Journal of The Royal Society Interface*. 2007;4(17):1107–  
655 1117. doi:10.1098/rsif.2007.0233.
- 656 [33] Simpson MJ, Treloar KK, Binder BJ, Haridas P, Manton KJ, Leavesley DI, et al. Quantifying the roles  
657 of cell motility and cell proliferation in a circular barrier assay. *Journal of The Royal Society Interface*.  
658 2013;10(82):20130007. doi:10.1098/rsif.2013.0007.
- 659 [34] Johnston ST, Ross JV, Binder BJ, McElwain DLS, Haridas P, Simpson MJ. Quantifying the effect of  
660 experimental design choices for in vitro scratch assays. *Journal of Theoretical Biology*. 2016;400:19–31.  
661 doi:10.1016/j.jtbi.2016.04.012.
- 662 [35] Jin W, Lo KY, Chou S, McCue SW, Simpson MJ. The role of initial geometry in experimental models of  
663 wound closing. *Chemical Engineering Science*. 2018;179:221–226. doi:10.1016/j.ces.2018.01.004.
- 664 [36] Lagergren JH, Nardini JT, Baker RE, Simpson MJ, Flores KB. Biologically-informed neural networks guide  
665 mechanistic modeling from sparse experimental data. *PLOS Computational Biology*. 2020;16(12):e1008462.  
666 doi:10.1371/journal.pcbi.1008462.
- 667 [37] Geris L, Lambrechts T, Carlier A, Papantoniou I. The future is digital: *in silico* tissue engineering. *Current  
668 Opinion in Biomedical Engineering*. 2018;6:92–98. doi:10.1016/j.cobme.2018.04.001.
- 669 [38] Sherratt JA, Murray JD. Models of epidermal wound healing. *Proceedings of the Royal Society of London  
670 Series B: Biological Sciences*. 1990;241(1300):29–36. doi:10.1098/rspb.1990.0061.
- 671 [39] Murray JD. Mathematical Biology. 3rd ed. Berlin: Springer-Verlag; 2002.
- 672 [40] Maini PK, McElwain DLS, Leavesley DI. Traveling wave model to interpret a wound-healing cell  
673 migration assay for human peritoneal mesothelial cells. *Tissue Engineering*. 2004;10(3-4):475–482.  
674 doi:10.1089/107632704323061834.
- 675 [41] Treloar KK, Simpson MJ. Sensitivity of edge detection methods for quantifying cell migration assays. *PLOS  
676 One*. 2013;8(6):e67389. doi:10.1371/journal.pone.0067389.
- 677 [42] Baldock AL, Ahn S, Rockne R, Johnston S, Neal M, Corwin D, et al. Patient-specific metrics of inva-  
678 siveness reveal significant prognostic benefit of resection in a predictable subset of gliomas. *PLOS One*.  
679 2014;9(10):e99057. doi:10.1371/journal.pone.0099057.

- 680 [43] Buttenschön A, Edelstein-Keshet L. Bridging from single to collective cell migration: A review of models and  
681 links to experiments. *PLOS Computational Biology*. 2020;16(12):e1008411. doi:10.1371/journal.pcbi.1008411.
- 682 [44] Gonçalves IG, Garcia-Aznar JM. Extracellular matrix density regulates the formation of tumour spheroids  
683 through cell migration. *PLOS Computational Biology*. 2021;17(2):e1008764. doi:10.1371/journal.pcbi.1008764.
- 684 [45] Browning AP, Jin W, Plank MJ, Simpson MJ. Identifying density-dependent interactions in collective cell  
685 behaviour. *Journal of The Royal Society Interface*. 2020;17(165):20200143. doi:10.1098/rsif.2020.0143.
- 686 [46] Yan XZ, Yang W, Yang F, Kersten-Niessen M, Jansen JA, Both SK. Effects of continuous passaging on  
687 mineralization of MC3T3-E1 cells with improved osteogenic culture protocol. *Tissue Engineering Part C:*  
688 *Methods*. 2014;20(3):198–204. doi:10.1089/ten.tec.2012.0412.
- 689 [47] Mathworks. Image Processing Toolbox: Regionprops; 2021. Available from: [www.mathworks.com/help/images/ref/regionprops.html](http://www.mathworks.com/help/images/ref/regionprops.html).
- 690 [48] Carroll RJ, Ruppert D. Transformation and Weighting in Regression. 1st ed. Boca Raton: Chapman and  
691 Hall; 1988.
- 692 [49] Hines KE, Middendorf TR, Aldrich RW. Determination of parameter identifiability in nonlinear  
693 biophysical models: A Bayesian approach. *The Journal of General Physiology*. 2014;143(3):401–16.  
694 doi:10.1085/jgp.201311116.
- 695 [50] Collis J, Connor AJ, Paczkowski M, Kannan P, Pitt-Francis J, Byrne HM, et al. Bayesian calibration,  
696 validation and uncertainty quantification for predictive modelling of tumour growth: a tutorial. *Bulletin of  
697 Mathematical Biology*. 2017;79(4):939–974. doi:10.1007/s11538-017-0258-5.
- 698 [51] Rackauckas C, Nie Q. DifferentialEquations.jl – A performant and feature-rich ecosystem for solving  
699 differential equations in Julia. *Journal of Open Research Software*. 2016;5(1). doi:10.5334/jors.151.
- 700 [52] Bezanson J, Edelman A, Karpinski S, Shah VB. Julia: a fresh approach to numerical computing. *SIAM  
701 Review*. 2017;59(1):65–98. doi:10.1137/141000671.
- 702 [53] Pawitan Y. In all likelihood: statistical modelling and inference using likelihood. Oxford: Oxford University  
703 Press; 2013.
- 704 [54] Johnson SG. The NLopt module for Julia; 2021.
- 705 [55] Jones DR, Perttunen CD, Stuckman BE. Lipschitzian optimization without the Lipschitz constant. *Journal  
706 of Optimization Theory and Applications*. 1993;79(1):157–181. doi:10.1007/bf00941892.
- 707 [56] Powell MJD. The BOBYQA algorithm for bound constrained optimization without derivatives. Cambridge,  
708 England: Department of Applied Mathematics and Theoretical Physics; 2009.
- 709 [57] Royston P. Profile likelihood for estimation and confidence intervals. *The Stata Journal*. 2007;7(3):376–387.  
710 doi:10.1177/1536867x0700700305.
- 711 [58] Venzon DJ, Moolgavkar SH. A method for computing profile-likelihood-based confidence intervals. *Applied  
712 Statistics*. 1988;37(1):87. doi:10.2307/2347496.
- 713 [59] Cai AQ, Landman KA, Hughes BD. Multi-scale modeling of a wound-healing cell migration assay. *Journal  
714 of Theoretical Biology*. 2007;245(3):576–594. doi:10.1016/j.jtbi.2006.10.024.
- 715 [60] Johnston ST, Shah ET, Chopin LK, McElwain DLS, Simpson MJ. Estimating cell diffusivity and cell  
716 proliferation rate by interpreting IncuCyte ZOOM™ assay data using the Fisher-Kolmogorov model. *BMC  
717 Systems Biology*. 2015;9(1):38. doi:10.1186/s12918-015-0182-y.
- 718 [61] Tarle V, Gauquelin E, Vedula SRK, D'Alessandro J, Lim CT, Ladoux B, et al. Modeling collective cell  
719 migration in geometric confinement. *Physical Biology*. 2017;14(3):035001. doi:10.1088/1478-3975/aa6591.
- 720 [62] Simpson MJ, Landman KA, Hughes BD, Newgreen DF. Looking inside an invasion wave of cells us-  
721 ing continuum models: Proliferation is the key. *Journal of Theoretical Biology*. 2006;243(3):343–360.  
722 doi:10.1016/j.jtbi.2006.06.021.
- 723 [63] Murphy RJ, Buenzli PR, Baker RE, Simpson MJ. A one-dimensional individual-based mechanical model of  
724 cell movement in heterogeneous tissues and its coarse-grained approximation. *Proceedings of the Royal Society  
725 A: Mathematical, Physical and Engineering Sciences*. 2019;475(2227):20180838. doi:10.1098/rspa.2018.0838.
- 726 [64] Hegarty-Cremer SGD, Simpson MJ, Andersen TL, Buenzli PR. Modelling cell guidance and curvature control  
727 in evolving biological tissues. *bioRxiv*. 2020;doi:10.1101/2020.07.10.197020.
- 728

